RSC Advances

PAPER

View Article Online
View Journal | View Issue

Open Access Article. Published on 05 January 2017. Downloaded on 2/7/2026 5:49:20 AM.
This article is licensed under a Creative Commons Attribution-NonCommercial 3.0 Unported Licence.

Cite this: *RSC Adv.*, 2017, 7, 1376

Achieving electroreduction of CO_2 to CH_3OH with high selectivity using a pyrite–nickel sulfide nanocomposite†

Siqi Zhao, Sijie Guo, Cheng Zhu, Jin Gao, Hao Li, Hui Huang,* Yang Liu*
and Zhenhui Kang*

Received 16th November 2016
Accepted 6th December 2016

DOI: 10.1039/c6ra26868d

www.rsc.org/advances

Electrochemical reduction of carbon dioxide (CO_2) to methanol (CH_3OH) catalyzed by transition metals has been proved feasible and effective in aqueous electrolytes. In this work, we introduce a FeS_2/NiS nanocomposite electrocatalyst synthesized by traditional hydrothermal method, which selectively reduces CO_2 to CH_3OH with an unprecedented overpotential of 280 mV and a high faradaic efficiency up to 64% at the potential of −0.6 V *vs.* reversible hydrogen electrode (RHE). The FeS_2/NiS nanocomposite electrocatalyst exhibits a stable current density of 3.1 mA cm^{-2} over a 4 hour stability test. The high selectivity towards CO_2 electroreduction to CH_3OH may be attributed to the special ladder structure of the FeS_2/NiS nanocomposite. The active sites are located at the interface between FeS_2 and NiS which can effectively suppress the side reaction hydrogen evolution reaction and facilitate the CO_2 reduction reaction.

Introduction

Electrochemical reduction of CO_2 to carbon-containing fuels is a feasible process which is conducive to solving the serious environmental problems caused by excess CO_2 such as iceberg melting, sea level rise and coastal delta subsidence.[1–3] However, the main defects of electroreduction CO_2 are the high overpotential required to drive the reaction, the low selectivity towards various products and the high cost of catalysts.[4,5] The high overpotential increases the consumption of energy and makes it difficult to achieve the sustainable transformation of CO_2. As for the selectivity, in addition to the major side reaction hydrogen evolution reaction (HER), the direct electroreduction of CO_2 in aqueous solution is able to generate diversiform carbon-containing chemicals.[5] The complex products increase the challenges towards generating target product. Transition metals are commonly proposed in CO_2 reduction reaction (CO_2RR) because of their vacant orbits and active d electrons.[5] Among them, Au,[6–9] Ag,[1,10,11] and Pd[12,13] have been explored comprehensively, while the expensive price limits the substantial application of noble metals in industry.[14] Moreover, the main product from noble metals is carbon monoxide (CO), which leads to the second pollution at the cost of CO_2 consumption.

CH_3OH, as an ideal chemical, is an important intermediate of paint, plastics, and other common products.[15] Besides, CH_3OH with high energy density can be stored as liquid under ambient conditions.[16,17] The standard potential of CO_2 electroreduction to CH_3OH is only 0.016 V (*vs.* RHE). However, the 6 e^- process of CO_2 reduction to form CH_3OH over the full reaction is kinetically unfavorable. Significant efforts towards selectively converting CO_2 into CH_3OH have been made since early 1983 over semiconductor materials (p-GaP and p-GaAs) with a low current density (<1 mA cm^{-2}).[18] Lately, Frese *et al.* firstly observed Teflon-supported Ru electrodes could selectively reduce CO_2 to CH_3OH with a low faradaic efficiency (FE) of 42%.[19] Fe,[20] Ni,[21] Cu[22] and their associated complexes[23–26] have been widely investigated in the yield of CO_2RR as their rich distribution and low cost. Among them, copper is demonstrated as the effective catalyst for the electroreduction of CO_2 to hydrocarbon and alcohols.[27,28] Le *et al.* reported that electrodeposited cuprous oxide thin films could directly reduce CO_2 to CH_3OH with a rate of 43 μmol cm^{-2} h^{-1} and low FE of 38%.[29] Therefore, it is urgent to seek for a highly active, selective and effective catalyst towards electroreduction CO_2 to CH_3OH.

Herein, we fabricated a low-cost FeS_2/NiS nanocomposite by traditional hydrothermal method as an excellent electrocatalyst. FeS_2/NiS nanocomposite displays incomparable operation in its low overpotential of 280 mV and high selectivity with a CH_3OH FE up to 64% at the potential of −0.6 V (*vs.* RHE). The stability test of FeS_2/NiS nanocomposite was performed for 4 hours, showing a stable current density of 3.1 mA cm^{-2} at −0.6 V (*vs.* RHE). There is no obvious degradation of the electrocatalyst after the long-time test. The following experiments reveal the

---

Jiangsu Key Laboratory for Carbon-Based Functional Materials & Devices, Institute of Functional Nano & Soft Materials (FUNSOM), Soochow University, 199 Ren'ai Road, Suzhou, 215123, Jiangsu, PR China. E-mail: zhkang@suda.edu.cn; yangl@suda.edu.cn; hhuang0618@suda.edu.cn

† Electronic supplementary information (ESI) available: The supplementary figures are shown. See DOI: 10.1039/c6ra26868d

This journal is © The Royal Society of Chemistry 2017

Open Access Article. Published on 05 January 2017. Downloaded on 2/7/2026 5:49:20 AM.
This article is licensed under a Creative Commons Attribution-NonCommercial 3.0 Unported Licence.

insight mechanism of CO_2RR catalyzed by FeS_2/NiS nanocomposite. As a comparison, we synthesized the single FeS_2 and NiS nanocrystals and applied in CO_2RR, respectively. The FeS_2 nanocrystal shows a negative onset potential at −0.45 V (*vs.* RHE) and a maximum current density of 4.2 mA cm^{-2} at −0.68 V (*vs.* RHE). The NiS nanocrystal shows a more negative onset potential at −0.5 V (*vs.* RHE) and extremely low current density of 1.0 mA cm^{-2} at −0.68 V (*vs.* RHE). Therefore, it can speculate that the active sites of the catalyst towards the process locate at the interface of FeS_2 and NiS. Besides, the FeS_2/NiS nanocomposite with an average diameter of 14 nm greatly increases the specific surface areas and the number of active sites.

Experiments

1. Materials

Ferric oxide (Fe_2O_3, 99%), nickel nitrate ($Ni(Ac)_2$, 99%), sulfur powder (99%), 1-octanol (99%), 1-octylamine (99%), ethanol (99.5%), $KHCO_3$ (99.7%) and Nafion perfluorinated resin solution (5 wt%) were purchased from Sigma-Aldrich and Adamas-beta; Nafion® 212 membrane was purchased from Dupont. Deionized water (purified by a Milli-Q system) was used to prepare all solutions and to rinse samples and glassware.

2. Instruments

The crystal structure of the catalyst was measured by X-ray diffraction (XRD) using an X'Pert-ProMPD (Holand) D/max-γAX-ray diffractometer with Cu Kα radiation ($\lambda = 0.154178$ nm). The high-resolution transmission electron microscopy (HRTEM) and scanning transmission electron microscopy (STEM) images were obtained using a FEI/Philips Tecnai G2 F20 TWIN transmission electron microscope. The Raman spectra were acquired with an HR 800 Raman spectroscope (J Y, France) equipped with a synapse CCD detector and a confocal Olympus microscope. X-ray photoelectron spectroscopy (XPS) was measured using a KRATOS Axis ultra-DLD X-ray photoelectron spectrometer with a monochromatised Mg Kα X-ray source ($h\nu = 1283.3$ eV). Scanning electron microscopy (SEM) images and energy dispersive X-ray (EDX) spectroscopy were performed by Carl Zeiss Supra 55 scanning electron microscope with an acceleration voltage of 20 kV. The electro-catalysis activities were measured by a Model CHI 660C workstation (CH Instruments, Chenhua, China).

3. Synthesis of catalyst

FeS_2/NiS nanocomposite. In a typical hydrothermal method,[30] Fe_2O_3 and $Ni(Ac)_2$ were introduced as iron and nickel sources, respectively. The ratio of nickel to iron is 1 : 1. Fe_2O_3 (2.5 mmol), $Ni(Ac)_2$ (2.5 mmol) and sulphur (50 mmol) were dissolved in 30.0 ml 1-octylamine and 30.0 ml 1-octanol at room temperature. Then, the mixture was transferred into a 150 ml stainless steel autoclave and heated to 260 °C for 3 hours under nitrogen atmosphere. When cooled to room temperature, the black precipitate was collected by centrifugation and thoroughly washed with ethanol for several times.

FeS_2 and NiS nanocrystals. The preparation of FeS_2 nanocrystal comes from the same hydrothermal method as FeS_2/NiS nanocomposite. 0.8 g Fe_2O_3 (5 mmol) and 1.6 g sulfur powder (50 mmol) were dissolved in 30.0 ml 1-octylamine and 30.0 ml 1-octanol at room temperature. Then, the mixture was transfer into a 150 ml stainless steel autoclave. The autoclave was sealed and heated to 260 °C for 3 hours under nitrogen atmosphere. The NiS nanocrystal was synthesized with the same hydrothermal method while changed the ratio of $Ni(Ac)_2$ and sulfur powder to 1 : 1.5.

4. Electrochemical measurements

The electrocatalytic activity measurements were performed in a standard three-electrode system. Saturated calomel electrode (SCE) was acted as the reference electrode with a standard electrode potential of 0.242 V (*vs.* RHE) and platinum wire was acted as the counter electrode. The working electrode was the catalyst modified glassy carbon disk electrode (GCE, 3.0 mm diameter CH Instruments) and 0.5 M $KHCO_3$ solution saturated with CO_2 was used as electrolyte. The cyclic voltammetry and linear sweep voltammetry were performed at a range from 0.7 to −0.7 V (*vs.* RHE) by a Model CHI 660C workstation under ambient condition. All the potentials reported here were *versus* $Hg/HgCl_2$ and were converted to the RHE scale using the Nernst equation:

$$E_{\mathrm{RHE}} = E_{\mathrm{Hg/HgCl_2}} + E^{\theta}_{\mathrm{Hg/HgCl_2}} + 0.0591 \times \mathrm{pH}_{\mathrm{electrolyte}}$$

E_{RHE} is the converted potential *versus* RHE. $E_{\mathrm{Hg/HgCl_2}}$ is the external potential measured against the $Hg/HgCl_2$ reference electrode. $E^{\theta}_{\mathrm{Hg/HgCl_2}}$ is the standard potential of $Hg/HgCl_2$ at 25 °C (0.242 V).

5. CO_2 reduction measurements and products quantification

The CO_2 reduction measurements were performed in an airtight electrochemical H-type cell under ambient temperature. The cathode compartment was consist of working electrode and reference electrode, while the anode compartment was composed of platinum wire. Apply dots of FeS_2/NiS nanocomposite catalyst (dissolved in 0.5% Nafion) to modified carbon fiber paper electrode (0.7 cm × 0.7 cm), then connect the carbon fiber paper to the cathode electrode. Each of the compartments loaded 75.0 ml 0.5 M $KHCO_3$ saturated with CO_2 and 40.0 ml carbon dioxide in the headspace. There is a slice of proton exchange membrane (Nafion® 212) at the connector to separate the two compartments in case the electroreduction products diffused to the anode. The electrolytic measurements were carried out under different potentials for 1 hour, respectively. The durability test was measured in an open electrolytic cell with 0.5 M $KHCO_3$ solution (saturated with CO_2) for 4 hours at −0.6 V. During the measurement, carbon dioxide was bubbled into water continuously with a uniform velocity. The carbon-contained gas products (CO, CH_4, C_2H_4, and C_2H_6) and major by-product (H_2) were tested by a thermal conductivity detector (TCD) with helium as the carrier gas. The liquid phase products were qualified by a NMR (Bruker AVANCEAV III 400)

Open Access Article. Published on 05 January 2017. Downloaded on 2/7/2026 5:49:20 AM.
This article is licensed under a Creative Commons Attribution-NonCommercial 3.0 Unported Licence.

spectroscopy, in which 0.5 ml electrolyte was mixed with 0.1 ml D_2O (deuterated water) and 0.05 μl dimethyl sulfoxide (DMSO, Sigma, 99.99%) was added as an internal standard.

The calculation of faradaic efficiency:

For CH_3OH,

$$\mathrm{FE}_{\mathrm{CH_3OH}} = \frac{6F \times n_{\mathrm{CH_3OH}}}{I \times t} \times 100\%$$

For H_2,

$$\mathrm{FE}_{\mathrm{H_2}} = \frac{2F \times n_{\mathrm{H_2}}}{I \times t} \times 100\%$$

where F is the Faraday constant, $n_{\mathrm{CH_3OH}}$ is the moles of produced CH_3OH, and $n_{\mathrm{H_2}}$ for the produced H_2.

Results and discussion

To explore the surface morphology of the FeS_2/NiS nanocomposite, the SEM measurement was carried out as shown in Fig. 1a. The acquired products are made up of uniform and even nanoparticles with an average diameter of approximately 14 nm. The small and even size of the electrocatalyst confirms high specific surface area and incremental active sites, which effectively improve the catalysis activity. The HRTEM image of FeS_2/NiS nanocomposite is shown in Fig. 1b. The characteristic lattice spacing of 0.27 nm is corresponding to the (200) plane of FeS_2 whose XRD peak is located at $2\theta = 33.0$.[30] The lattice spacing of 0.29 nm is indexed to the (100) plane of the NiS which matches to the XRD peak at $2\theta = 46.0$.[31] Fig. 1c shows the STEM image and corresponding chemical mappings of Fe–K, Fe–L, Ni–K, Ni–L and S–K for FeS_2/NiS nanocomposite. A homogeneous distribution of Fe, Ni, and S is reviewed in the nanocomposite. Furthermore, the HRTEM image concludes that the germination of FeS_2/NiS nanocomposite arranges intimately rather than the simple physical mixture of the two compounds. Thus, we proposed that the active sites of CO_2 electroreduction locate at the interface between FeS_2 (200) and NiS (100).

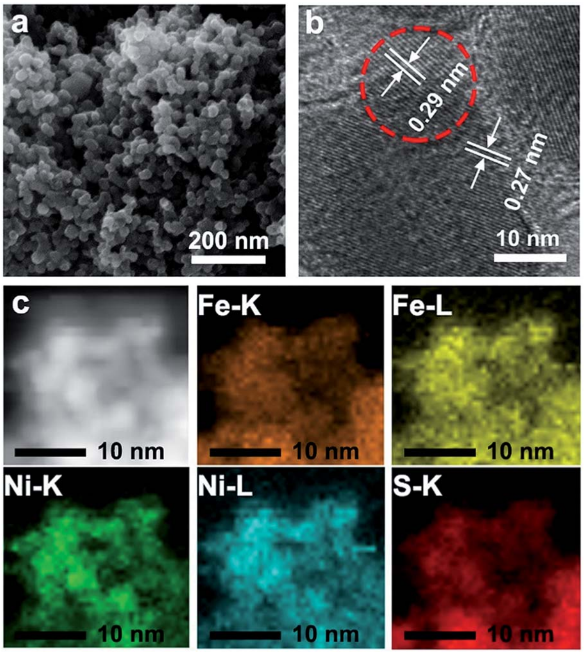

Fig. 1 (a) The SEM image of FeS_2/NiS nanocomposite. (b) The HRTEM image of FeS_2/NiS nanocomposite. (c) STEM image and corresponding chemical elements mappings of Fe–K, Fe–L, Ni–K, Ni–L and S–K of FeS_2/NiS nanocomposite.

In order to identify the crystallinity and structure of the FeS_2/NiS nanocomposite, the XRD measurements were performed. Fig. 2a shows the XRD patterns of FeS_2/NiS nanocomposite (brown trace), FeS_2 standard card (blue trace) and NiS standard card (red trace). The phanic peaks can be completely matched to the FeS_2 (JCPDS no. 42-1340) and NiS (JCPDS no. 02-1280) standard diffraction peaks. In details, the predominant peaks at 46.0, 53.7, 30.2 and 34.7 degree correspond to the (100), (202), (101) and (102) planes of NiS, respectively. The peaks at 33.0, 56.4, 37.1 and 47.5 degree are assigned to the (200), (311), (210) and (211) planes of FeS_2, respectively. There are no impurity peaks from other crystal structures. The average size of FeS_2/NiS nanocomposite is ~14 nm from the line width analysis of the diffraction peak calculated by Scherer equation, which is consistent with the SEM observation. FeS_2/NiS nanocomposite was further characterized with Raman spectrum and showed in Fig. 2b. The peaks at 340 and 378 cm^{-1} can be well attributed to Raman vibrations of pyrite FeS_2 and no other impurity peaks from marcasite and troilite.[30] The peaks at 222 and 285 cm^{-1} are matching with NiS completely.[32] The peaks assigned to NiS at 335 and 376 cm^{-1} are not emerged in the diagram obviously, which is resulted by the overlap with the peaks of pyrite FeS_2.

The XPS measurement was introduced to confirm the element proportion and valence state of the FeS_2/NiS nanocomposite. Besides the Fe, Ni and S elements from FeS_2/NiS nanocomposite, C and O elements are also detected in the full spectrum (as shown in Fig. 3a). The elements of C and O may attribute to the carbonization of the solvents. The high resolution spectra of C 1s and O 1s are shown in Fig. S1.† The binding energy at 284.8, 286.4 and 288.8 eV of C 1s are consistent with graphite carbon, C–OH and C=O, respectively.[33] The O 1s peaks at 531.9 and 532.9 eV from oxygen atoms are attributed to C=O and O–C, respectively.[34] The carbonized solvents with oxygenic functional groups may not only improve the stability of the

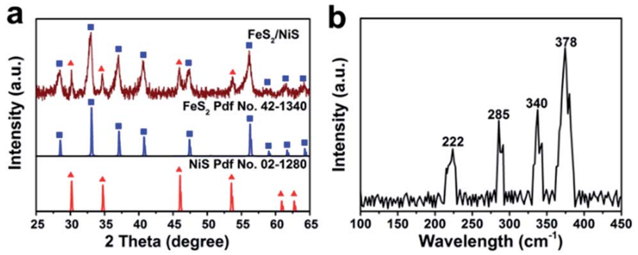

Fig. 2 (a) The large-angle XRD patterns of FeS_2/NiS nanocomposite (brown trace), FeS_2 (blue trace) and NiS (red trace). (b) Raman spectrum of FeS_2/NiS nanocomposite.

This journal is © The Royal Society of Chemistry 2017

Open Access Article. Published on 05 January 2017. Downloaded on 2/7/2026 5:49:20 AM.
This article is licensed under a Creative Commons Attribution-NonCommercial 3.0 Unported Licence.

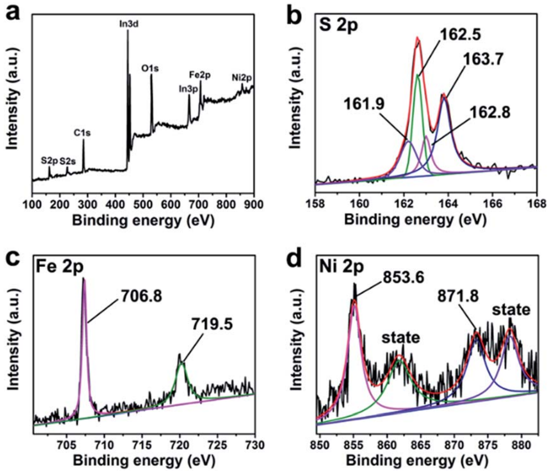

Fig. 3 (a) The full XPS spectrum of FeS_2/NiS nanocomposite and the high-resolution XPS spectra of (b) S 2p, (c) Fe 2p and (d) Ni 2p.

catalyst but also act as a support.[35] The high resolution scan spectra of the Fe 2p, Ni 2p and S 2p are presented in Fig. 3b–d. The atomic ratio of Fe to Ni is equal to 2 according to the XPS calculation. The result is consistent with the EDX spectroscopy measurement (as shown in Fig. S2†). The binding energy at 706.8 and 719.5 eV are conformed to the Fe $2p^{3/2}$ and Fe $2p^{1/2}$ which are characterized of pyrite.[36] The Ni $2p^{3/2}$ and Ni $2p^{1/2}$ peaks are observed at 853.6 and 871.8 eV, exist two satellite peaks at 858.7 and 878.1 eV respectively,[32] indicating that the nickel existed in bivalent states. There are four peaks in the high resolution XPS spectra of S. The S $2p^{3/2}$ and S $2p^{1/2}$ peaks located at 161.9 and 162.8 eV are consistent with S^{2-},[31] while the peaks at 162.5 and 163.7 eV are identified with the S $2p^{3/2}$ and S $2p^{1/2}$ of $S_2{}^{2-}$.[37] These results indicate that both $S_2{}^{2-}$ and S^{2-} are existed. Thus, we integrate the peak areas respectively and acquire the ratio of $S_2{}^{2-}$ to S^{2-} is 2, which is also consistent with the previously calculated ratio of iron to nickel.

In typical experiments, the electrolytic activities were measured in a three-electrode system in 0.5 M $KHCO_3$ aqueous solution. The curves of Linear Sweep Voltammetry (LSV) for the FeS_2/NiS nanocomposite are shown in Fig. 3a. The black curve shows the catalytic activity for HER under N_2 atmosphere (pH = 8.5), which presents a high overpotential over 450 mV and a low current density of 2.5 mA cm^{-2} with the applied potential up to −0.68 V. In comparison, an obvious enhancement of current density of 7.8 mA cm^{-2} is observed at the potential of −0.68 V when the electrolyte is saturated with CO_2 (pH = 7.5). The onset potential performs more positive at −0.30 V, indicating a low overpotential less than 280 mV (confirmed by GC and ^1H NMR). The results reveal that the electrocatalyst can selectively reduce CO_2 and suppress the HER efficiently under CO_2 atmosphere.

As a comparison, we investigated the electrocatalytic performances of FeS_2 nanocrystal and NiS nanocrystal for CO_2 electroreduction, respectively. The detailed synthetic process is shown in Experiment section. The specific characterizations including XRD, SEM and TEM of the as-prepared FeS_2 and NiS nanocrystals are shown in Fig. S3 and S4.† The LSVs of FeS_2, NiS and FeS_2/NiS were measured in CO_2-saturated 0.5 M $KHCO_3$ solution. As showed in Fig. 4b, both the single FeS_2 and NiS nanocrystals show poor activities towards CO_2RR compared with FeS_2/NiS nanocomposite, in which the FeS_2 shows an onset potential at −0.45 V for HER and the maximum current density of 4.2 mA cm^{-2} at −0.68 V. While the NiS nanocrystal performs even worse, which shows an extremely low current density of 1 mA cm^{-2} at −0.68 V (red trace). It is generally known that FeS_2 is feasible towards HER.[38,39] For FeS_2/NiS nanocomposite (black trace), more positive onset potential at −0.3 V as well as higher current density of 7.8 mA cm^{-2} can be achieved towards CO_2RR.

To further compare the electrocatalytic performance of FeS_2 nanocrystal, NiS nanocrystal and FeS_2/NiS nanocomposite for CO_2 reduction, the electrolytic reduction reaction of CO_2 was carried out in an electrochemical airtight H-type cell at the potential range from −0.3 to −0.7 V. The gas products were detected by gas chromatography (GC). The liquid-phase products were detected by ^1H NMR and the DMSO was added as an internal standard. As shown in Fig. S5,† the reduced products are CH_3OH after CO_2 electroreduction catalyzed by FeS_2/NiS nanocomposite for 2 hours and 4 fours. For FeS_2 and NiS nanocrystals, H_2 is the only product in gas phase and no hydrocarbon products are detected in both gas and liquid phases. As shown in Fig. 4c, the FEs *vs.* the applied potentials (−0.5, −0.6, −0.7 V) of H_2 for FeS_2 and NiS nanocrystals show a stable tendency at different potentials. For FeS_2/NiS nanocomposite, the FEs *vs.* the applied potentials (−0.3, −0.4, −0.5, −0.6, −0.7 V) for CH_3OH (left axis) and H_2 (right axis) are shown in Fig. 4d. The CH_3OH FEs show an overall growth tendency at the range from −0.3 V to −0.6 V but reach a plateau of 64% approximately at −0.6 V. After that, it maintains a stable tendency. We further compared the FEs for CH_3OH in the literatures and showed in Table S1.† To reach the same FE of

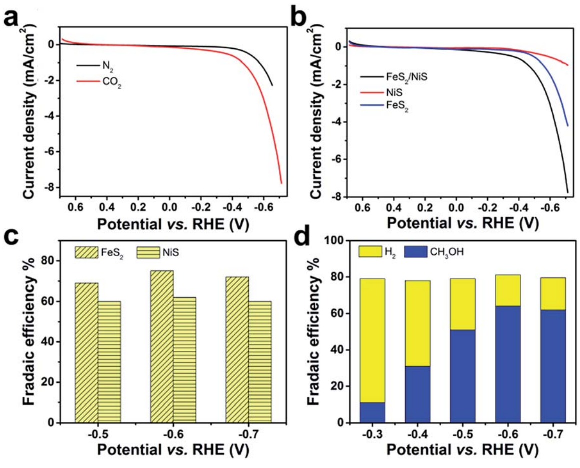

Fig. 4 (a) LSVs of FeS_2/NiS nanocomposite in 0.5 M $KHCO_3$ aqueous solution under N_2 (blue trace) and CO_2 (red trace) atmosphere; (b) LSVs of FeS_2/NiS nanocomposite (black trace), NiS (red trace), and FeS_2 (blue trace) in 0.5 M $KHCO_3$ aqueous solution under CO_2 atmosphere; (c) faradaic efficiencies *vs.* potential of H_2 for FeS_2 and NiS nanocrystals; (d) faradaic efficiencies *vs.* potential of CH_3OH and H_2 for FeS_2/NiS nanocomposite.

Open Access Article. Published on 05 January 2017. Downloaded on 2/7/2026 5:49:20 AM.
This article is licensed under a Creative Commons Attribution-NonCommercial 3.0 Unported Licence.

CH_3OH, FeS_2/NiS nanocomposite shows a moderate potential compared with those noble metal electrocatalysts. The H_2 FEs for FeS_2/NiS nanocomposite show an opposite tendency compared with CH_3OH. The FEs of H_2 continuously decreases and decreases to a minimum of 17% at the applied potential of −0.6 V. Moreover, the total FEs for the generation of CH_3OH and H_2 are maintained at 81% over the whole process. These results demonstrate that single FeS_2 and NiS nanocrystals can hardly reduce CO_2 into hydrocarbon products, whereas the FeS_2/NiS nanocomposite can achieve an efficient and selective electroreduction process for CO_2. Thus, we propose the active sites for CO_2RR locate at the interface between FeS_2 and NiS.

To further prove the stability of the FeS_2/NiS nanocomposite, the continuous tendency test was measured in a standard three-electrode cell as shown in Fig. 5a. A stable current density of 3.1 mA cm^{-2} is observed over the 4 hours electroreduction at the potential of −0.6 V. Besides, the FE of the products (CH_3OH and H_2) for the FeS_2/NiS nanocomposite is maintained at about 81% over the 4 hours electrolysis. It can observe no obvious deactivation of FeS_2/NiS nanocomposite for CO_2 reduction throughout the entire process. Then, the XRD measurement was performed on the reacted FeS_2/NiS nanocomposite as shown in Fig. 5b. The XRD analysis indicates that there is no transformation taking place upon the catalyst during the whole electroreduction. These results fully confirm that FeS_2/NiS nanocomposite is excellently stable and efficient for CO_2 electroreduction.

To understand the highly efficient electrocatalysis activity of FeS_2/NiS nanocomposite, we further compared the performances of CO_2RR catalysed by FeS_2/NiS nanocomposite, pure FeS_2 and NiS nanocrystals. The single FeS_2 and NiS nanocrystals show poor activities towards CO_2RR. The FeS_2 nanocrystal shows a negative onset potential at −0.45 V and the maximum current density of 4.2 mA cm^{-2} at −0.68 V. Then, the NiS nanocrystal shows a more negative onset potential at −0.5 V and extremely low current density of 1 mA cm^{-2} at −0.68 V. Furthermore, a physical mixture of FeS_2 and NiS nanocrystals with the same ratio as FeS_2/NiS nanocomposite was fabricated. The electrocatalytic activity for CO_2 reduction was measured and showed in Fig. S6.† The current density presents a slight increasement under CO_2 atmosphere compared with N_2 atmosphere. Then, a 2 h-electrolysis in 0.5 M CO_2-saturated $KHCO_3$ for the physical mixture was performed at the potential of −0.6 V. Only H_2 was detected in the both gas phase and liquid phase products. The increasement of current density may be ascribed to the effect of pH. In contrast, the FeS_2/NiS nanocomposite exhibits excellent activity for CO_2RR. It achieves an unprecedented overpotential of 280 mV and a stable current density of 3.1 mA cm^{-2} at the potential of −0.6 V. Comparing the electrocatalytic performances of CO_2RR in FeS_2 nanocrystal, NiS nanocrystal, physical mixture of FeS_2 and NiS nanocrystals and FeS_2/NiS nanocomposite, it can speculate that the active sites of the catalyst locate at the interface between FeS_2 (200) and NiS (100) (as shown in Fig. 6). On the other hand, many researches have evidenced that the electroreduction of CO_2 to CH_3OH is a complex process which includes the transformation of 6 e^- and 6 H^+.[5,37–40] Still, more experimental and theoretical calculations are needed to unravel the detailed mechanism of this multistep reaction.

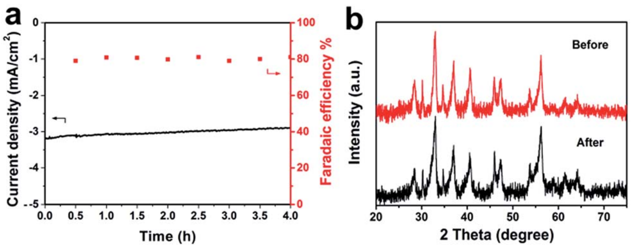

Fig. 5 (a) Stability of FeS_2/NiS nanocomposite for CO_2 reduction operated at a potential of −0.6 V *vs.* RHE for 4 hours. Geometric current density *vs.* time (left axis) and total FE for production (CH_3OH and H_2) *vs.* time (right axis); (b) the large-angle XRD patterns of FeS_2/NiS nanocomposite before (red trace) and after (black trace) 4 hours electroreduction.

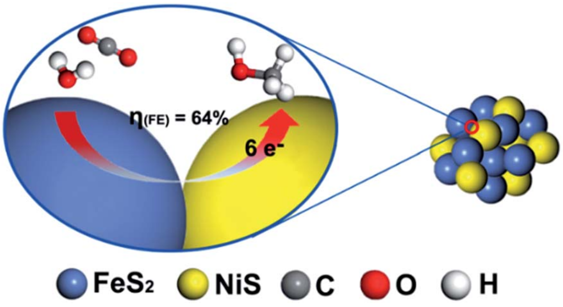

Fig. 6 The proposed reaction mechanism of electroreduction CO_2 by FeS_2/NiS nanocomposite electrocatalyst.

Conclusion

We synthesized the FeS_2/NiS nanocomposite with a traditional hydrothermal method. It was demonstrated that FeS_2/NiS nanocomposite can catalyze CO_2RR at an unprecedented overpotential of 280 mV and a high CH_3OH faradaic efficiency up to 64% at the potential of −0.6 V. Moreover, the catalyst performs a stable current density of 3.1 mA cm^{-2} over the 4 hours stability test and there is no obvious degradation after electroreduction from XRD observation. In experiments, the FeS_2 nanocrystals, NiS nanocrystals and the physical mixture of FeS_2 and NiS nanocrystals all show poor activity towards CO_2RR, while the FeS_2/NiS nanocomposite exhibits excellent activity towards the process. Thus, the high activity and selectivity towards CO_2 electroreduction to CH_3OH is probably attributed to the special ladder structure of the FeS_2/NiS nanocomposite. The active sites may locate at the interface between FeS_2 and NiS which could effectively suppress the side reaction of HER and facilitate the CO_2RR. The low-cost FeS_2/NiS nanocomposite is an efficient alternative to expensive materials for the application of CO_2 electroreduction in industry.

Acknowledgements

This work is supported by the Collaborative Innovation Center of Suzhou Nano Science and Technology, the National Natural

Open Access Article. Published on 05 January 2017. Downloaded on 2/7/2026 5:49:20 AM. This article is licensed under a Creative Commons Attribution-NonCommercial 3.0 Unported Licence.

Science Foundation of China (51422207, 51132006, 51572179, 21471106, 21501126), the Specialized Research Fund for the Doctoral Program of Higher Education (20123201110018), a Suzhou Planning Project of Science and Technology (ZXG2012028), and a project funded by the Priority Academic Program Development of Jiangsu Higher Education Institutions (PAPD).

Notes and references

1 Q. Lu, J. Rosen, Y. Zhou, G. S. Hutchings, Y. C. Kimmel, J. G. Chen and F. Jiao, *Nat. Commun.*, 2014, **5**, 3242.
2 R. Reske, H. Mistry, F. Behafarid, B. Roldan Cuenya and P. Strasser, *J. Am. Chem. Soc.*, 2014, **136**, 6978–6986.
3 J. Wu, R. M. Yadav, M. Liu, P. P. Sharma, C. S. Tiwary, L. Ma, X. Zou, X.-D. Zhou, B. I. Yakobson, J. Lou and P. M. Ajayan, *ACS Nano*, 2015, **9**, 5364–5371.
4 J. O. Bockris, *J. Electrochem. Soc.*, 1989, **136**, 2521.
5 J. Qiao, Y. Liu, F. Hong and J. Zhang, *Chem. Soc. Rev.*, 2014, **43**, 631–675.
6 W. Zhu, R. Michalsky, Ö. Metin, H. Lv, S. Guo, C. J. Wright, X. Sun, A. A. Peterson and S. Sun, *J. Am. Chem. Soc.*, 2013, **135**, 16833–16836.
7 S. Back, M. S. Yeom and Y. Jung, *ACS Catal.*, 2015, **5**, 5089–5096.
8 H. Mistry, R. Reske, Z. Zeng, Z.-J. Zhao, J. Greeley, P. Strasser and B. R. Cuenya, *J. Am. Chem. Soc.*, 2014, **136**, 16473–16476.
9 W. Zhu, Y.-J. Zhang, H. Zhang, H. Lv, Q. Li, R. Michalsky, A. A. Peterson and S. Sun, *J. Am. Chem. Soc.*, 2014, **136**, 16132–16135.
10 J. Rosen, G. S. Hutchings, Q. Lu, S. Rivera, Y. Zhou, D. G. Vlachos and F. Jiao, *ACS Catal.*, 2015, **5**, 4293–4299.
11 S. Ma, R. Luo, J. I. Gold, A. Z. Yu, B. Kim and P. J. A. Kenis, *J. Mater. Chem. A*, 2016, **4**, 8573–8578.
12 D. Gao, H. Zhou, J. Wang, S. Miao, F. Yang, G. Wang, J. Wang and X. Bao, *J. Am. Chem. Soc.*, 2015, **137**, 4288–4291.
13 X. Wang, H. Shi, J. H. Kwak and J. Szanyi, *ACS Catal.*, 2015, **5**, 6337–6349.
14 Y. Gong, Y. Zhao, Y. Chen, Y. Wang and C. Sun, *RSC Adv.*, 2016, **6**, 43185–43190.
15 J. Albo, M. Alvarez-Guerra, P. Castaño and A. Irabien, *Green Chem.*, 2015, **17**, 2304–2324.
16 C. Zhai, M. Zhu, F. Pang, D. Bin, C. Lu, M. C. Goh, P. Yang and Y. Du, *ACS Appl. Mater. Interfaces*, 2016, **8**, 5972–5980.
17 C. Zhai, M. Zhu, D. Bin, F. Ren, C. Wang, P. Yang and Y. Du, *J. Power Sources*, 2015, **275**, 483–488.
18 D. Canfield and K. W. Frese, *J. Electrochem. Soc.*, 1983, **130**, 1772.
19 K. W. Frese and S. Leach, *J. Electrochem. Soc.*, 1985, **132**, 259–260.
20 K. Hara, A. Kudo and T. Sakata, *J. Electroanal. Chem.*, 1995, **386**, 257–260.
21 A. Kudo, S. Nakagawa, A. Tsuneto and T. Sakata, *J. Electrochem. Soc.*, 1993, **140**, 1541–1545.
22 K. Hara, A. Tsuneto, A. Kudo and T. Sakata, *J. Electrochem. Soc.*, 1994, **141**, 2097–2103.
23 S. Bagherzadeh and N. P. Mankad, *J. Am. Chem. Soc.*, 2015, **137**, 10898–10901.
24 G. Kyriacou and A. Anagnostopoulos, *J. Electroanal. Chem.*, 1992, **322**, 233–246.
25 J. B. Varley, H. A. Hansen, N. L. Ammitzbøll, L. C. Grabow, A. A. Peterson, J. Rossmeisl and J. K. Nørskov, *ACS Catal.*, 2013, **3**, 2640–2643.
26 A. B. Bocarsly, Q. D. Gibson, A. J. Morris, R. P. L'Esperance, Z. M. Detweiler, P. S. Lakkaraju, E. L. Zeitler and T. W. Shaw, *ACS Catal.*, 2012, **2**, 1684–1692.
27 H. Mistry, A. S. Varela, C. S. Bonifacio, I. Zegkinoglou, I. Sinev, Y.-W. Choi, K. Kisslinger, E. A. Stach, J. C. Yang, P. Strasser and B. R. Cuenya, *Nat. Commun.*, 2016, **7**, 12123.
28 D. Raciti, K. J. Livi and C. Wang, *Nano Lett.*, 2015, **15**, 6829–6835.
29 M. Le, M. Ren, Z. Zhang, P. T. Sprunger, R. L. Kurtz and J. C. Flake, *J. Electrochem. Soc.*, 2011, **158**, E45.
30 B.-B. Yu, X. Zhang, Y. Jiang, J. Liu, L. Gu, J.-S. Hu and L.-J. Wan, *J. Am. Chem. Soc.*, 2015, **137**, 2211–2214.
31 J. Yuan, J. Wen, Y. Zhong, X. Li, Y. Fang, S. Zhang and W. Liu, *J. Mater. Chem. A*, 2015, **3**, 18244–18255.
32 J. S. Chen, J. Ren, M. Shalom, T. Fellinger and M. Antonietti, *ACS Appl. Mater. Interfaces*, 2016, **8**, 5509–5516.
33 L. Bai, S. Qiao, Y. Fang, J. Tian, J. Mcleod, Y. Song, H. Huang, Y. Liu and Z. Kang, *J. Mater. Chem. C*, 2016, **4**, 8490–8495.
34 B. Y. Yu and S.-Y. Kwak, *J. Mater. Chem.*, 2012, **22**, 8345.
35 H. Li, X. Zhang and D. R. MacFarlane, *Adv. Energy Mater.*, 2015, **5**, 1401077.
36 F. Jiang, L. T. Peckler and A. J. Muscat, *Cryst. Growth Des.*, 2015, **15**, 3565–3572.
37 R. Morrish, R. Silverstein and C. A. Wolden, *J. Am. Chem. Soc.*, 2012, **134**, 17854–17857.
38 D.-Y. Wang, M. Gong, H.-L. Chou, C.-J. Pan, H.-A. Chen, Y. Wu, M.-C. Lin, M. Guan, J. Yang, C.-W. Chen, Y.-L. Wang, B.-J. Hwang, C.-C. Chen and H. Dai, *J. Am. Chem. Soc.*, 2015, **137**, 1587–1592.
39 D. Jasion, J. M. Barforoush, Q. Qiao, Y. Zhu, S. Ren and K. C. Leonard, *ACS Catal.*, 2015, **5**, 6653–6657.
40 A. Roldan and N. H. de Leeuw, *Faraday Discuss.*, 2016, **188**, 161–180.